Nanoscale

ROYAL SOCIETY OF CHEMISTRY

PAPER

View Article Online
View Journal | View Issue

Cite this: *Nanoscale*, 2025, **17**, 20096

Co-doped RuIr nanoparticles for enhanced activity and stability in alkaline overall water splitting

Zhuofan Gan,[a] Jingwen Cao,[a] Zhixu Chen,[b] Peixi Qiu,[a] Jiangyun Bai,[a] Chengyong Shu*[a] and Wei Tang *[a,b]

Developing highly active and stable bifunctional electrocatalysts for overall water splitting is critical for sustainable hydrogen production. Herein, the introduction of Co dopants into RuIr alloys resulted in a comprehensive enhancement of both HER and OER activities and stability. Co dopants tuned the electronic structure of Ru/Ir, optimizing the hydrogen binding energy and weakening the OH adsorption ability on Ru/Ir active sites, thereby enhancing HER performance. Co-$Ru_{0.55}Ir_{0.45}O_x$ required only a 21.2 mV overpotential to achieve 10 mA cm^{-2}, with a Tafel slope of 27.9 mV dec^{-1} and a TOF of 7.18 H_2 per s (at −0.15 V *vs.* RHE) in the alkaline HER. Additionally, the electrochemical dissolution of Co and the increase in oxygen vacancies promoted the formation of oxygen-deficient Ru/Ir–O_v species, which are identified as the actual active sites for the OER, thereby initiating a continuous metal site–oxygen vacancy synergistic mechanism (MS-O_vSM). In this pathway, two OH^- species nucleophilically attack the adjacent Ru/Ir–O_v pair and directly couple to form *O–O* intermediates, thus improving OER activity. Co-$Ru_{0.55}Ir_{0.45}O_x$ exhibited an overpotential of 242 mV at 10 mA cm^{-2}, with a Tafel slope of 41.8 mV dec^{-1}, and a TOF of 3.23 O_2 per s (at 1.60 V *vs.* RHE) in alkaline solution. The d–d orbital interactions between Co and RuIr facilitated the electron transfer from Co to Ir and Ru, suppressing particle agglomeration and the dissolution of Ru/Ir species due to severe oxidation, thereby enhancing stability. The constructed Co-$Ru_{0.55}Ir_{0.45}O_x$||Co-$Ru_{0.55}Ir_{0.45}O_x$ electrolyzer achieved 10 mA cm^{-2} at a potential of 1.51 V, demonstrating its potential application in overall water splitting.

Received 27th May 2025,
Accepted 1st August 2025

DOI: 10.1039/d5nr02238j

rsc.li/nanoscale

Introduction

The effective production of hydrogen *via* overall water splitting is considered one of the most promising pathways for renewable energy generation.[1] The successful electrochemical conversion of water into hydrogen is heavily reliant on efficient electrocatalysts for both the hydrogen and oxygen evolution reactions (HER/OER), which are energy-intensive processes that demand significant overpotentials to proceed.[2] Because the dominant OER electrocatalysts at the anode are highly susceptible to severe degradation in acidic environments, alkaline water electrolysis presents a more promising industrial route for large-scale green hydrogen production.[3] Although platinum-based catalysts have demonstrated exceptional HER activity, their high cost and sluggish reaction kinetics in alkaline solutions limit their large-scale application.[4] On the other hand, the most commonly used OER catalysts currently are RuO_2 or IrO_2, which suffer from low stability and high overpotentials under alkaline conditions due to their strong binding energy with oxygen-containing intermediates, making them less efficient for sustainable water splitting.[5] Since both the HER and OER are complex processes involving multiple steps and electron transfers, they result in considerable voltage gaps.[6] Therefore, developing bifunctional electrocatalysts that can simultaneously improve the activity and stability of the alkaline HER and OER is essential for enhancing the overall efficiency of water splitting.

In recent years, ruthenium (Ru)-based catalysts have gained attention as viable substitutes for platinum (Pt) due to their lower cost and comparable Gibbs free energy change of H* (ΔG_{H^*}) in the HER.[7] Nevertheless, the intense interaction between Ru 4d and H 1s orbitals often leads to an excessively high binding energy of Ru–H, hindering the efficient adsorption and desorption of H.[8] In addition, the robust binding of hydroxide (OH) with Ru impedes the transfer of OH_{ad} ($OH_{ad} + e^- \rightarrow OH^-$), resulting in the poisoning of Ru sites and consequently limiting the water dissociation efficiency.[9,10] On the other hand, while Ru-based catalysts are recognized for their outstanding OER activity, their long-term stability under operating conditions remains a major challenge, limiting their

[a]*School of Chemical Engineering and Technology, Xi'an Jiaotong University, Xi'an 710049, P. R. China. E-mail: kowscy-n@mail.xjtu.edu.cn, tangw2018@xjtu.edu.cn*
[b]*National Innovation Platform (Center) for Industry-Education Integration of Energy Storage Technology, Xi'an Jiaotong University, Xi'an 710049, P. R. China. E-mail: tangw2018@xjtu.edu.cn*

practical application. The surface of Ru is prone to excessive oxidation during the OER process, leading to the formation of soluble RuO_4^{2-}, which consequently reduces the stability of the catalyst.[11] Additionally, the strong binding energy between lattice oxygen and oxygen-containing intermediates slows down the reaction kinetics.[12] Therefore, developing Ru-based bifunctional electrocatalysts to address the aforementioned issues is crucial for the practical application of water electrolysis in hydrogen production. Recent studies have shown that the binding strength between Ru and H/OH can be modulated by adjusting the electronic structure of Ru 4d orbitals. Alloying Ru with iridium (Ir), which has a higher work function, helps optimize the electronic structure of Ru, thereby achieving an optimal Ru–H binding energy that accelerates the HER kinetics.[13] At the same time, the alloying process weakens Ru's adsorption of OH, which facilitates the exposure of more unblocked active sites for water dissociation.[14] Additionally, due to the superior corrosion resistance of Ir-based materials, an "Ir protective framework" can form on the surface of RuIr particles, effectively inhibiting Ru dissolution during the OER process.[15,16] For example, Qiao *et al.* reported a core–shell structured Ru@IrO_x nanocrystal that exhibits both enhanced OER activity and stability. This improvement is attributed to the charge redistribution at the interface, which effectively maintains the stability of the Ru/Ir oxidation states.[17] Doping RuIr electrocatalysts with transition metals possessing partially filled d-orbitals can further enhance their catalytic activity. The strong d–d orbital interactions can regulate the redistribution of electron density on the catalyst surface, thereby optimizing the adsorption energies of reaction intermediates (such as H*, OH*, O*, and OOH*), which in turn improves the reaction kinetics.[18,19] However, the intrinsic mechanism by which transition metals affect the activity and stability of RuIr catalysts for overall water splitting is not yet fully understood.

In this work, we have introduced a Co-doped RuIr alloy electrocatalyst with superior performance in both the HER and OER under alkaline conditions. The Co dopants altered the electronic structure of Ru/Ir, optimizing the hydrogen binding energy and reducing the OH adsorption strength on the active sites of Ru/Ir, thus enhancing HER performance. Furthermore, the electrochemical dissolution of Co and the formation of oxygen vacancies promoted the creation of low-coordinated oxygen species (O^{I-}) on the RuIr alloy surface. These electrophilic O^{I-} species facilitated the nucleophilic attack of H_2O, leading to the fast generation of OOH_{ads}, thereby improving OER activity. The Co-$Ru_{0.55}Ir_{0.45}O_x$ electrocatalyst exhibited a low overpotential of 21.2 mV to achieve 10 mA cm^{-2}, with a Tafel slope of 27.9 mV dec^{-1} and a TOF of 7.18 H_2 per s (at −0.15 V *vs.* RHE) in the alkaline HER. This electrocatalyst demonstrated an overpotential of only 278 mV at 10 mA cm^{-2}, with a Tafel slope of 41.8 mV dec^{-1} and a TOF of 2.08 O_2 per s (at 1.60 V *vs.* RHE) in the alkaline OER. Additionally, the d–d orbital interactions between Co and RuIr promoted electron transfer from Co to Ir and Ru, which suppressed particle aggregation and the dissolution of Ru/Ir species caused by severe oxidation, thus enhancing the catalyst's stability. The Co-$Ru_{0.55}Ir_{0.45}O_x$||Co-$Ru_{0.55}Ir_{0.45}O_x$ electrolyzer achieved a current density of 10 mA cm^{-2} at a low potential of 1.51 V and demonstrated stable operation for over 60 h at various current densities, highlighting its potential application value in overall water splitting.

Results and discussion

Morphology and structure characterization of catalysts

The Co-$Ru_{0.55}Ir_{0.45}O_x$ alloy particles were synthesized *via* the polyol reflux method, and the detailed experimental procedure is provided in the SI. Transmission electron microscopy (TEM) images revealed that the particles exhibited a segmented lotus root-like morphology (Fig. 1a), a morphology similar to that observed in $Ru_{0.55}Ir_{0.45}O_x$ alloys (Fig. S1a). High-resolution TEM (HR-TEM) images of region 1 in Fig. 1a show lattice spacings of 0.216 nm and 0.222 nm, corresponding to the $(01\bar{1}0)$ plane of hcp-RuIr and the (111) plane of fcc-RuIr, respectively (Fig. 1b). Region 2 in Fig. 1a corresponds to the junction between particles, resembling the "internodes" of the lotus root. The HR-TEM image (Fig. 1c) shows that the particles at the top exhibited lattice spacings of 0.199 nm and 0.216 nm, corresponding to the $(10\bar{1}1)$ and $(01\bar{1}0)$ planes of the hcp-RuIr alloy. The particles at the bottom displayed a larger lattice spacing (0.222 nm), corresponding to the (111) plane of the fcc-RuIr alloy. The diffraction spots obtained from the Fourier transform of the TEM images also confirm the coexistence of hcp and fcc phases in RuIr alloys. A similar heterogeneous structure was observed in $Ru_{0.55}Ir_{0.45}O_x$ alloy particles as well (Fig. S1b). We hypothesize that the formation of this distinctive structure is attributed to the differing reduction rates of Ru^{3+} and Ir^{4+}: H_2Cl_6Ir undergoes reduction more readily than $RuCl_3$ in ethylene glycol solution, leading to the preferential nucleation of hexagonal Ir-rich crystal seeds with fcc-(111) facets. These Ir-enriched seeds then serve as nucleation centers, facilitating the epitaxial growth of hcp-phase RuIr alloys by reducing the energy required for nucleation and growth.[20] The distinctive lotus root-like heterogeneous structure significantly expands the surface area of alloys, promoting the exposure of additional active sites and improving the accessibility of molecules for electrocatalytic processes.[21] The uniform distribution of Co, Ru, and Ir elements across the entire particle range in the EDS images confirms the formation of Co-doped RuIr alloy particles (Fig. 1d and Fig. S2). Similarly, the overlap of Ru and Ir elements in the $Ru_{0.55}Ir_{0.45}O_x$ sample confirms the formation of the RuIr alloys (Fig. S3). The mass fractions as well as the atomic ratios of Ru and Ir were further determined by inductively coupled plasma atomic emission spectroscopy (ICP-AES) (Table S1). The results indicate that the atomic ratio of Ru to Ir in both Co-$Ru_{0.55}Ir_{0.45}O_x$ and $Ru_{0.55}Ir_{0.45}O_x$ samples was approximately 55 : 45.

The powder X-ray diffraction (XRD) pattern shows that Co-$Ru_{0.55}Ir_{0.45}O_x$ nanoparticles exhibited the strongest diffraction peak at 41.62°, with the peak position located between the strongest peaks of Ru (JCPDS: PDF#65-1863) and Ir (JCPDS:

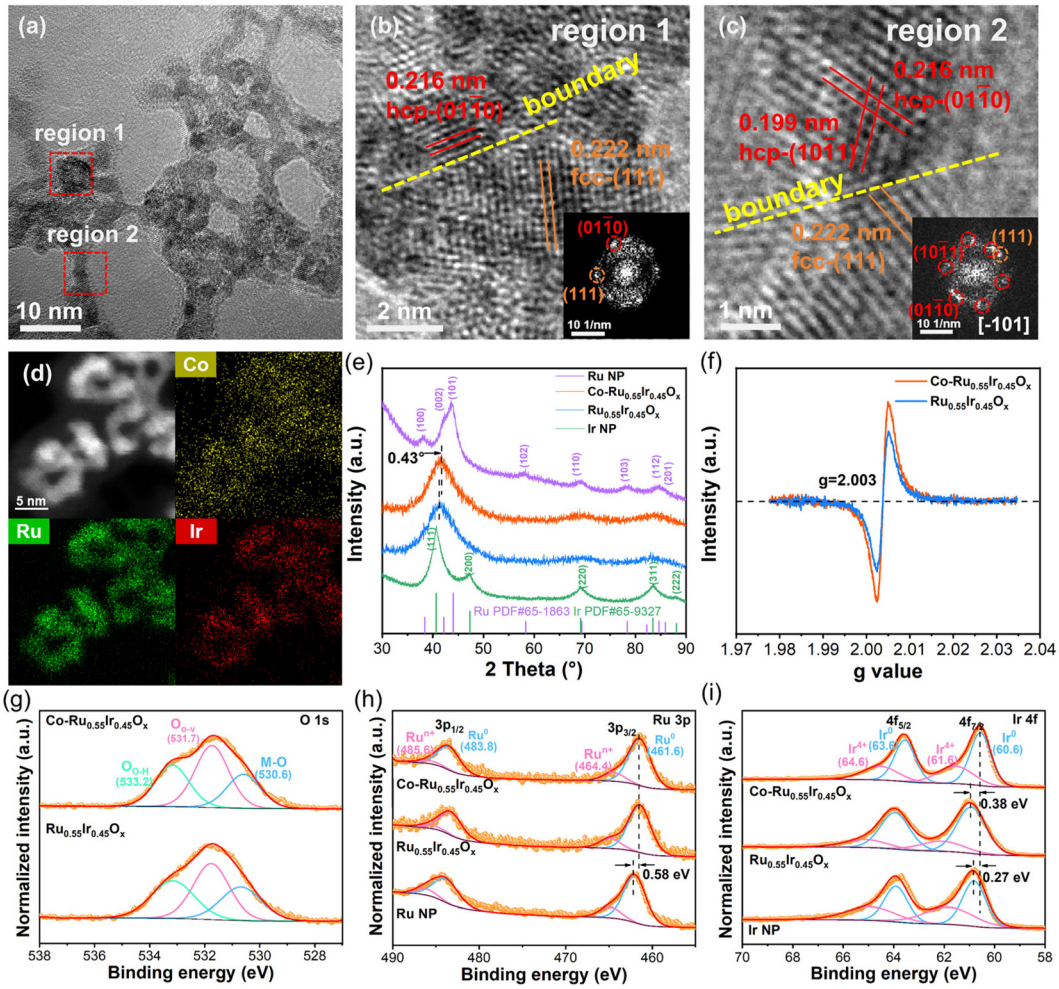

Fig. 1 (a) TEM and (b and c) HR-TEM images of Co-$Ru_{0.55}Ir_{0.45}O_x$. (d) EDS mappings of Co-$Ru_{0.55}Ir_{0.45}O_x$. (e) XRD patterns of Co-$Ru_{0.55}Ir_{0.45}O_x$, $Ru_{0.55}Ir_{0.45}O_x$, Ru and Ir nanoparticles. (f) EPR spectra of Co-$Ru_{0.55}Ir_{0.45}O_x$ and $Ru_{0.55}Ir_{0.45}O_x$. XPS spectra of (g) O 1s, (h) Ru 3p and (i) Ir 4f orbitals.

PDF#65-9327) (Fig. 1e). For Ru_xIr_{1-x} alloys, as the Ru component increased, the strongest diffraction peak of the RuIr alloy shifted from 40.64° to 43.75°, indicating the formation of the RuIr alloy (Fig. S4). The XRD patterns of Co-$Ru_{0.55}Ir_{0.45}O_x$ and $Ru_{0.55}Ir_{0.45}O_x$ were similar, with the peak position shifting 0.43° towards higher angles for Co-$Ru_{0.55}Ir_{0.45}O_x$. This suggests that Co doping does not alter the crystal structure of the RuIr alloy but generates a compressive strain effect due to the smaller atomic radius of Co (126 pm) compared to Ru (132 pm) and Ir (136 pm). The electron paramagnetic resonance (EPR) results show that both catalysts exhibited a peak at g = 2.003, indicating the presence of oxygen vacancies in both catalysts, which may have been introduced by unavoidable surface oxidation.[22] The peak intensity of Co-$Ru_{0.55}Ir_{0.45}O_x$ was higher than that of $Ru_{0.55}Ir_{0.45}O_x$, suggesting that Co doping increased the concentration of oxygen vacancies in the RuIr alloy due to its lower resistance to oxidative corrosion (Fig. 1f).

X-ray photoelectron spectroscopy (XPS) was used to investigate the surface valence states and electronic structure of the catalysts. The XPS survey spectra exhibit elemental signals consistent with the precursor composition, confirming the successful synthesis of the catalysts (Fig. S5). In addition, the Co 2p spectrum of Co-$Ru_{0.55}Ir_{0.45}O_x$ shows an unacceptable signal-to-noise ratio (Fig. S6) due to the low Co content (2.93 wt%), making it difficult to be detected by the low-energy X-ray source (Al Kα: 1486.6 eV). The O 1s spectra were fitted into three components: M–O (M = Ru, Ir and Co) at 530.6 eV, oxygen vacancies ($O_{O\text{-}V}$) at 531.7 eV, and O–H species ($O_{O\text{–}H}$) at 533.2 eV (Fig. 1g). Compared to $Ru_{0.55}Ir_{0.45}O_x$, the Co-$Ru_{0.55}Ir_{0.45}O_x$ sample exhibited a decreased M–O content and an increased $O_{O\text{-}V}$ content (Fig. S7), indicating that Co doping reduced the surface lattice oxygen of the RuIr alloys while enhancing the concentration of oxygen vacancies, which is consistent with the EPR results.[23] The high-resolution Ru 3p spectra revealed the presence of both Ru^0 and Ru^{n+} valence states in the catalysts. The Ru 3p spectra of Co-$Ru_{0.55}Ir_{0.45}O_x$ can be deconvoluted into $3p_{3/2}$ (461.6 eV) and $3p_{1/2}$ (483.8 eV) of Ru^0 components, as well as Ru^{n+} components at $3p_{3/2}$ (464.4 eV) and $3p_{1/2}$ (485.6 eV), indicating the presence of surface-oxidized RuO_x species (Fig. 1h).[24,25] Additionally, compared to Ru

nanoparticles, both Co-$Ru_{0.55}Ir_{0.45}O_x$ and $Ru_{0.55}Ir_{0.45}O_x$ samples showed a negative shift (0.58 eV) of binding energy for Ru, suggesting that the formation of the RuIr alloy increases the electron cloud density of Ru. Although Co doping exerted minimal influence on the Ru 3p XPS features, the Ru 3d spectra revealed a 0.15 eV negative shift in the Ru $3d_{5/2}$ peak upon Co incorporation, suggesting an increased electron density on Ru induced by Co doping (Fig. S8). The Ir 4f spectra of Co-$Ru_{0.55}Ir_{0.45}O_x$ were deconvoluted into $4f_{7/2}$ (60.6 eV) and $4f_{5/2}$ (63.6 eV) of Ir^0, as well as Ir^{4+} $4f_{7/2}$ (61.6 eV) and $4f_{5/2}$ (64.6 eV), indicating the coexistence of metallic Ir and IrO_x species (Fig. 1i).[14] Additionally, in the $Ru_{0.55}Ir_{0.45}O_x$ sample, the binding energy of Ir was shifted positively by 0.11 eV compared to Ir nanoparticles. Combining this with the changes in the Ru valence state, it can be concluded that alloying promotes electron transfer from Ir to Ru. More importantly, compared to $Ru_{0.55}Ir_{0.45}O_x$, Co-$Ru_{0.55}Ir_{0.45}O_x$ exhibited a negative binding energy shift of 0.38 eV, suggesting that Co doping facilitates electron transfer from Co to Ir due to the strong d–d orbital interaction.[18] We propose that Co doping facilitates electron transfer along the Co → Ir → Ru pathway and increases the concentration of oxygen vacancies, thereby providing a theoretical basis for optimizing the adsorption energies of HER/OER intermediates and enhancing the overall catalytic performance.

Evaluation of HER performance

The catalyst's performance for the hydrogen evolution reaction (HER) was evaluated in a H_2-saturated 1 M KOH electrolyte with a three-electrode system. Initially, a series of Ru_xIr_{1-x} catalysts were synthesized and their HER performances were systematically evaluated to determine the optimal Ru/Ir atomic ratio. The polarization curves revealed that the $Ru_{0.55}Ir_{0.45}$ catalyst exhibited the best HER performance (Fig. S10), which was attributed to its moderate hydrogen binding energy (HBE) and more active sites unoccupied by adsorbed OH_{ad}. The hydrogen underpotential deposition (H_{upd}) peak potential in CV curves reflects the HBE of the active sites, while the charge of the H_{upd} peak (Q_H) corresponds to the amount of H_{ad} on the active sites (Fig. S11a). The results indicate that, with increasing Ir content in the Ru_xIr_{1-x} alloys, the H_{upd} peak potential shifts positively, implying an enhancement in the Ru/Ir–H binding strength. However, a weak HBE is unfavorable for water dissociation, while an excessively strong HBE hinders the desorption of H_{ad} and the subsequent formation of H_2. Additionally, Q_H displayed a volcano-shaped trend with increasing Ir content, reaching a maximum at the $Ru_{0.55}Ir_{0.45}$ catalyst, suggesting the highest number of accessible active sites for water dissociation at this ratio (Fig. S11b). Therefore, the Ru : Ir atomic ratio was fixed at 0.55 : 0.45 in the subsequent study to systematically evaluate the influence of Co doping on the catalytic performance. To optimize the Co doping ratio, we systematically varied the $CoCl_2$ precursor amount (3.1–30.8 mg) during synthesis and characterized the resulting electrocatalysts. The polarization curves exhibited a distinct volcano-type relationship between HER activity and $CoCl_2$ content, with peak catalytic performance achieved at an optimal $CoCl_2$ dosage of 7.7 mg (Fig. S12). Remarkably, this optimal composition also exhibited superior oxygen evolution reaction (OER) activity in an O_2-saturated electrolyte (Fig. S13), demonstrating exceptional bifunctional catalytic properties. Consequently, we established 7.7 mg as the optimal $CoCl_2$ dosage for all subsequent research.

Linear sweep voltammetry (LSV) revealed that the Co-$Ru_{0.55}Ir_{0.45}O_x$ catalyst exhibited the highest activity, achieving a current density of 10 mA cm^{-2} at an overpotential of 21.2 mV, which is lower than the 23.3 mV for $Ru_{0.55}Ir_{0.45}O_x$ and 33.3 mV for the commercial Pt/C catalyst (Fig. 2a and b). And its performance approaches or even surpasses that of recently reported Ru/Ir-based catalysts (Table S2). The results from the accelerated degradation tests (ADTs) show that after 5000 CV cycles, the Co-$Ru_{0.55}Ir_{0.45}O_x$ catalyst exhibited a minimal increase in overpotential of only 4.2 mV at a current density of 150 mA cm^{-2}, which is significantly lower than the 16.9 mV for $Ru_{0.55}Ir_{0.45}O_x$ and 10.2 mV for commercial Pt/C. At a potential of −0.10 V *vs.* RHE, the mass activity of the Co-$Ru_{0.55}Ir_{0.45}O_x$ reached 6.90 A mg_{PGM}^{-1}, approximately 1.93 times higher than that of $Ru_{0.55}Ir_{0.45}O_x$ (3.58 A mg_{PGM}^{-1}) and 7.34 times greater than that of commercial Pt/C (0.94 A mg_{PGM}^{-1}). These results indicate that the introduction of Co atoms significantly enhances both the activity and stability for the HER. The electrochemically active surface areas (ECSAs) of the electrocatalysts were determined from the double-layer capacitance (C_{dl}). As shown in Fig. S14 and Table S3, Co-$Ru_{0.55}Ir_{0.45}O_x$ exhibited a higher C_{dl} value (43.3 mF cm^{-2}) and ECSA (1082.5 cm^2), indicating that Co doping increased the concentration of oxygen vacancies and introduced the strain effect at the atomic level, which collectively increased the ECSA of the catalyst.[18,26] The ECSA-normalized LSV curves reflect the intrinsic activity of the catalysts (Fig. S15). The results suggest that the Co-$Ru_{0.55}Ir_{0.45}O_x$ catalyst exhibited superior specific activity compared to $Ru_{0.55}Ir_{0.45}O_x$. The Tafel slopes were derived from the LSV curves and used to study the reaction kinetics of the catalysts. The Tafel slope for Co-$Ru_{0.55}Ir_{0.45}O_x$ was calculated to be 27.9 mV dec^{-1}, which was lower than that of $Ru_{0.55}Ir_{0.45}$ (32.7 mV dec^{-1}) and Pt/C (44.4 mV dec^{-1}) (Fig. 2c). The similar Tafel slopes suggest that all electrocatalysts follow the Volmer–Heyrovsky mechanism for the HER, where the rate-determining step is the sluggish dissociation of water molecules (Volmer step: $H_2O + e^- \rightarrow H_{ad} + OH^-$).[27] Exchange current density (j_0) values of the catalysts were obtained by applying the extrapolation method to the Tafel plots (Fig. S16). Co-$Ru_{0.55}Ir_{0.45}O_x$ displayed a higher j_0 value of 3.181 mA cm^{-2} compared to 2.142 mA cm^{-2} for $Ru_{0.55}Ir_{0.45}O_x$. These results indicate that Co doping boosts the catalytic activity and reaction kinetics of the HER.[28,29] At a potential of −0.15 V *vs.* RHE, the turnover frequency (TOF) of Co-$Ru_{0.55}Ir_{0.45}O_x$ reached a maximum value of 7.18 H_2 per s, approximately 4.08 times higher than that of commercial Pt/C (1.76 H_2 per s) and 1.67 times higher than $Ru_{0.55}Ir_{0.45}O_x$ (4.29 H_2 per s), further confirming the superior intrinsic HER activity of the Co-$Ru_{0.55}Ir_{0.45}O_x$ catalyst (Fig. 2d).

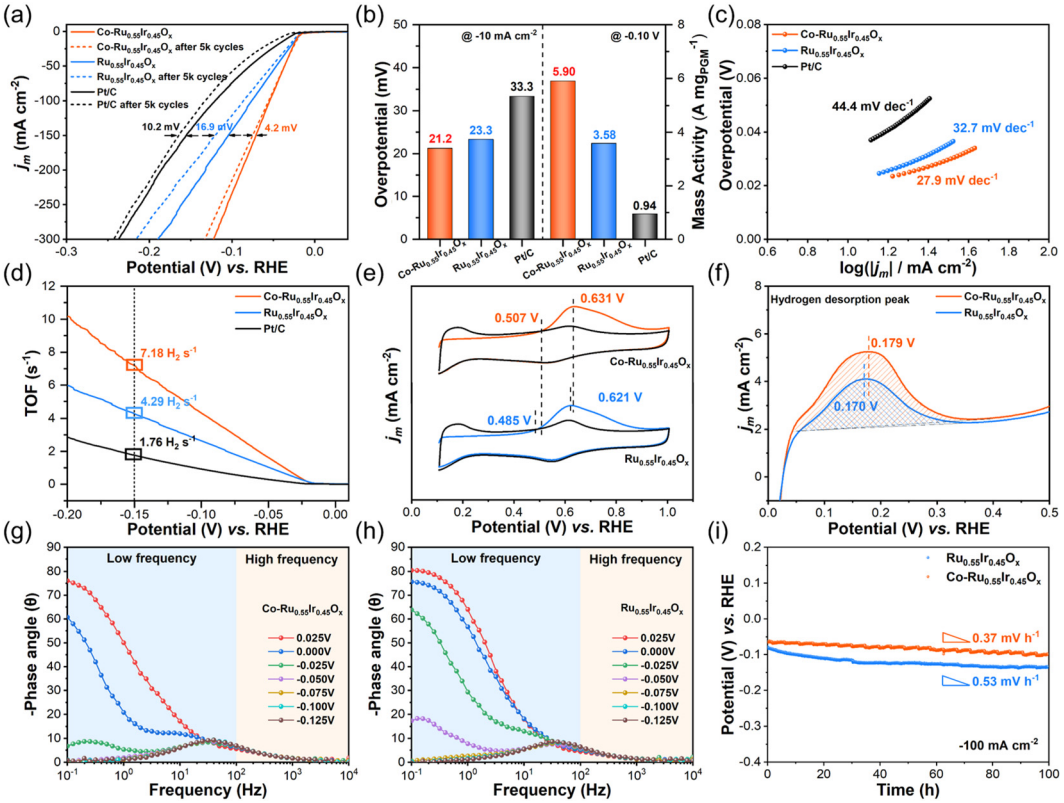

Fig. 2 Hydrogen evolution reaction (HER) performance of Co-$Ru_{0.55}Ir_{0.45}O_x$ and $Ru_{0.55}Ir_{0.45}O_x$ in 1 M KOH solution: (a) polarization curves before and after 5k CV sweeps between −0.4 and 0.1 V (*vs.* RHE) at a scan rate of 100 mV s^{-1}. (b) Overpotential required to obtain 10 mA cm^{-2} (left panel) and the mass activity at a potential of −0.10 V *vs.* RHE (right panel) for Co-$Ru_{0.55}Ir_{0.45}O_x$, $Ru_{0.55}Ir_{0.45}O_x$ and commercial Pt/C. (c) Tafel slope, (d) turnover frequency, (e) CO-stripping analysis, and (f) the hydrogen desorption region determined by cyclic voltammetry. Phase images in Bode plots of (g) Co-$Ru_{0.55}Ir_{0.45}O_x$ and (h) $Ru_{0.55}Ir_{0.45}O_x$ under different voltages. (i) Stability test recorded at a constant current density of 100 mA cm^{-2}.

To investigate the reason for the improved HER performance with Co doping, the CO stripping method was first employed to examine the OH adsorption ability on the active sites, as adsorbed OH_{ad} facilitates the oxidation of adsorbed CO (CO_{ad}) to CO_2 ($OH_{ad} + CO_{ad} \rightarrow CO_2 + H^+ + e^-$).[30] As shown in Fig. 2e, the Co-$Ru_{0.55}Ir_{0.45}O_x$ catalyst exhibited higher onset (0.507 V *vs.* RHE) and peak potentials (0.631 V *vs.* RHE) for CO oxidation compared to $Ru_{0.55}Ir_{0.45}O_x$, indicating that Co doping weakens the OH adsorption strength on the Ru/Ir active sites. The reduced OH adsorption promotes the rapid transfer of OH_{ad} generated in the Volmer step from the active sites to the electrolyte, thus providing more unoccupied active sites for the HER.[31] The H_{upd} peak potential of Co-$Ru_{0.55}Ir_{0.45}O_x$ (0.179 V *vs.* RHE) was slightly higher than that of $Ru_{0.55}Ir_{0.45}O_x$ (0.170 V *vs.* RHE), suggesting that the Co dopants slightly strengthen the HBE on the Ru/Ir active sites, which effectively promotes water dissociation during the Volmer step. Additionally, the Q_H of Co-$Ru_{0.55}Ir_{0.45}O_x$ was larger than that of $Ru_{0.55}Ir_{0.45}O_x$, which can be attributed to the inhibition of the occupation of active sites by OH_{ad} due to Co doping, thus exposing more active sites for water dissociation (Fig. 2f).[32]

Operando EIS tests were conducted at different applied potentials to reveal the adsorption/desorption dynamics of intermediates on the catalyst surface. As shown in Fig. S17, Co-$Ru_{0.55}Ir_{0.45}O_x$ exhibited the same ohmic resistance (R_s) as $Ru_{0.55}Ir_{0.45}O_x$, indicating that the conductivity of the catalyst remains unchanged. However, Co-$Ru_{0.55}Ir_{0.45}O_x$ displayed a lower charge transfer resistance (R_{ct}) at all applied potentials, suggesting that Co doping accelerates charge transfer during the reaction process. Notably, the phase angle in the Bode-phase plot at low frequencies (<100 Hz) reflects charge transfer at the electrode–electrolyte interface.[33] Compared to $Ru_{0.55}Ir_{0.45}O_x$, Co-$Ru_{0.55}Ir_{0.45}O_x$ showed a rapid decrease in the phase angle within a potential range of −0.025 to −0.050 V *vs.* RHE, demonstrating that Co dopants promote charge transfer at the electrode–electrolyte interface and accelerate the HER kinetics (Fig. 2g and h). The enhanced HER performance is attributed to the electronic structure modulation of Ru/Ir induced by Co dopants *via* d–d orbital hybridization, optimizing H and OH adsorption on Ru/Ir sites. Electron transfer from Co to Ir resulted in a downward shift of the d-band center of Ir (away from the Fermi level), weakening the H_{ad} and OH_{ad} adsorption on Ir sites, while a slight upshift of Ru's d-band center enhanced the Ru–H binding strength.[23] These effects promoted the dissociation of H_2O and the subsequent desorption of H_{ad} to form H_2 on Ru/Ir sites. Meanwhile, the weakened OH_{ad} adsorption facilitated

its rapid removal into the electrolyte, thus exposing more active sites for sustained H_2O dissociation during the Volmer step.

In addition to the excellent HER activity, the Co-$Ru_{0.55}Ir_{0.45}O_x$ catalyst demonstrates outstanding HER stability. After operating stably for 100 h at a current density of 100 mA cm^{-2}, Co-$Ru_{0.55}Ir_{0.45}O_x$ exhibited only a 0.37 mV h^{-1} potential decay, which was lower than that of $Ru_{0.55}Ir_{0.45}O_x$ (0.53 mV h^{-1}) (Fig. 2i). We hypothesize that the robust HER stability arises from the strong d–d orbital hybridization between Co and Ru/Ir atoms, which enhances the structural stability of the RuIr crystal, thereby suppressing the agglomeration and leaching of the less crystalline Ru/Ir atoms during the reaction process.[34]

The changes in the surface elemental valence states of the catalysts after stability tests were investigated by XPS. For both Co-$Ru_{0.55}Ir_{0.45}O_x$ and $Ru_{0.55}Ir_{0.45}O_x$, the XPS spectra of Ru 3p and Ir 4f orbitals exhibited positive shifts in binding energy, indicating varying degrees of surface oxidation of the RuIr alloys after long-term chronoamperometry measurements. The decrease in the electron density around Ru and Ir atoms hampers the electron transfer to H_2O for the formation of H_{ad}, thus deteriorating the HER activity of both electrocatalysts.[4] However, The Ru 3p orbital shift was significantly attenuated in Co-$Ru_{0.55}Ir_{0.45}O_x$ (ΔBE = 0.99 eV) compared to the undoped $Ru_{0.55}Ir_{0.45}O_x$ (ΔBE = 1.47 eV) (Fig. 3a and b). Similarly, the Ir 4f orbital in Co-$Ru_{0.55}Ir_{0.45}O_x$ showed a smaller positive shift of 0.57 eV, significantly lower than that in $Ru_{0.55}Ir_{0.45}O_x$ (Fig. 3c and d). These results suggest that electron transfer from Co to Ru/Ir *via* d–d orbital hybridization partially suppresses the oxidation of Ru and Ir during HER operation, thereby enhancing catalytic stability.

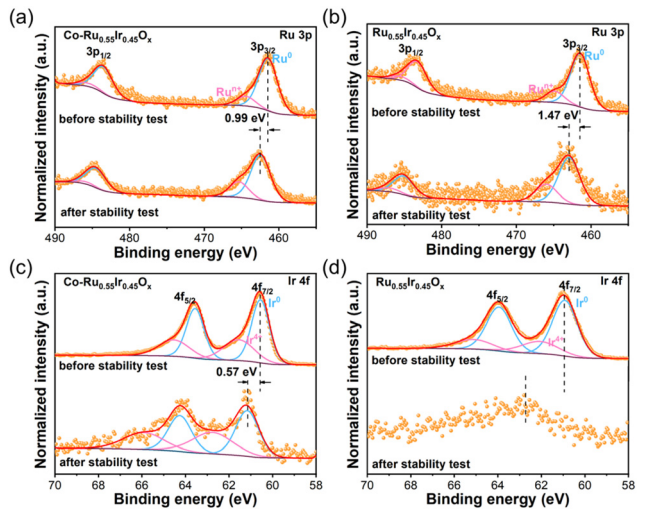

Fig. 3 XPS spectra of Ru 3p of (a) Co-$Ru_{0.55}Ir_{0.45}O_x$ and (b) $Ru_{0.55}Ir_{0.45}O_x$ before and after the HER stability test. XPS spectra of Ir 4f of (c) Co-$Ru_{0.55}Ir_{0.45}O_x$ and (d) $Ru_{0.55}Ir_{0.45}O_x$ before and after the HER stability test.

Evaluation of OER performance

The OER performance of the catalysts was evaluated in O_2-saturated 1 M KOH solution. Fig. 4a shows the polarization curves of the catalysts, indicating that the Co-$Ru_{0.55}Ir_{0.45}O_x$ catalyst exhibited the best performance, requiring an overpotential of only 242 mV to reach a current density of 10 mA cm^{-2}, which was lower than those of $Ru_{0.55}Ir_{0.45}O_x$ (253 mV) and commercial RuO_2 (280 mV). At a potential of 1.60 V *vs.* RHE, the mass activity of Co-$Ru_{0.55}Ir_{0.45}O_x$ reached 9.24 mg_{PGM}^{-1} (Fig. 4b), which was *ca.* 1.49 times higher than that of $Ru_{0.55}Ir_{0.45}O_x$ (6.21 A mg_{PGM}^{-1}) and 23.10 times higher than that of commercial RuO_2 (0.40 A mg_{PGM}^{-1}). ADT results show that after 5000 (5k) cycles at a scan rate of 100 mV s^{-1} in the potential range of 1.2–1.8 V *vs.* RHE, the overpotential of Co-$Ru_{0.55}Ir_{0.45}O_x$ increased by only 2.5 mV when the current density reached 150 mA cm^{-2}, significantly lower than those of $Ru_{0.55}Ir_{0.45}O_x$ (29.9 mV) and commercial RuO_2 (7.8 mV). The higher stability of commercial RuO_2 is attributed to its stable crystal structure.[35] In contrast, the poor stability of $Ru_{0.55}Ir_{0.45}O_x$ is due to the small particle size and poor crystallinity of the alloy particles synthesized by the polyol reflux method, leading to particle agglomeration and inevitable dissolution of Ru/Ir atoms during the OER process. These results demonstrate that Co doping effectively enhances the catalytic activity and stability of the OER catalyst. The catalyst's ECSAs were calculated from the C_{dl}, and the results showed that the ECSA of Co-$Ru_{0.55}Ir_{0.45}O_x$ was 437.5 cm^{-2}, *ca.* 1.27 times that of $Ru_{0.55}Ir_{0.45}O_x$ (345.0 cm^{-2}), which is attributed to the compressive strain introduced at the atomic level by Co doping (Fig. S18 and Table S5). The ECSA-normalized LSV curves show that the specific activity of the Co-$Ru_{0.55}Ir_{0.45}O_x$ catalyst was superior to that of $Ru_{0.55}Ir_{0.45}O_x$ (Fig. S19). The Tafel slope of Co-$Ru_{0.55}Ir_{0.45}O_x$ (41.8 mV dec^{-1}) was lower than those of $Ru_{0.55}Ir_{0.45}O_x$ (45.6 mV dec^{-1}) and commercial RuO_2 (61.6 mV dec^{-1}), indicating that Co-$Ru_{0.55}Ir_{0.45}O_x$ exhibited faster OER kinetics (Fig. 4c). Additionally, at a potential of 1.60 V *vs.* RHE, the TOF value of Co-$Ru_{0.55}Ir_{0.45}O_x$ reached 3.23 O_2 per s, approximately 1.43 times that of $Ru_{0.55}Ir_{0.45}O_x$ (2.26 O_2 per s) and 32.30 times that of RuO_2 (0.10 O_2 per s), further confirming the excellent intrinsic OER activity of Co-$Ru_{0.55}Ir_{0.45}O_x$ (Fig. 4d). It is noteworthy that we observed a significant change in the CV curves of Co-$Ru_{0.55}Ir_{0.45}O_x$ and $Ru_{0.55}Ir_{0.45}O_x$ catalysts after 5k cycles in the OER working potential range (Fig. S20). To elucidate this phenomenon, we recorded the LSV and corresponding CV curves of Co-$Ru_{0.55}Ir_{0.45}O_x$ from 0 to 40 cycles (Fig. S21). The results show that the CV curves of Co-$Ru_{0.55}Ir_{0.45}O_x$ gradually changed during the continuous electrochemical cycling and reached a stable shape after 30 cycles. Meanwhile, the LSV curves revealed that the OER activity of the catalyst improved with increasing number of testing cycles and reached its stable activity after 30 cycles. These results indicate that surface reconstruction and dynamic evolution of the active species occurred in Co-$Ru_{0.55}Ir_{0.45}O_x$ during the OER.[36,37] ICP-OES was used to determine the concentrations of Co, Ru, and Ir dissolved in the electrolyte after

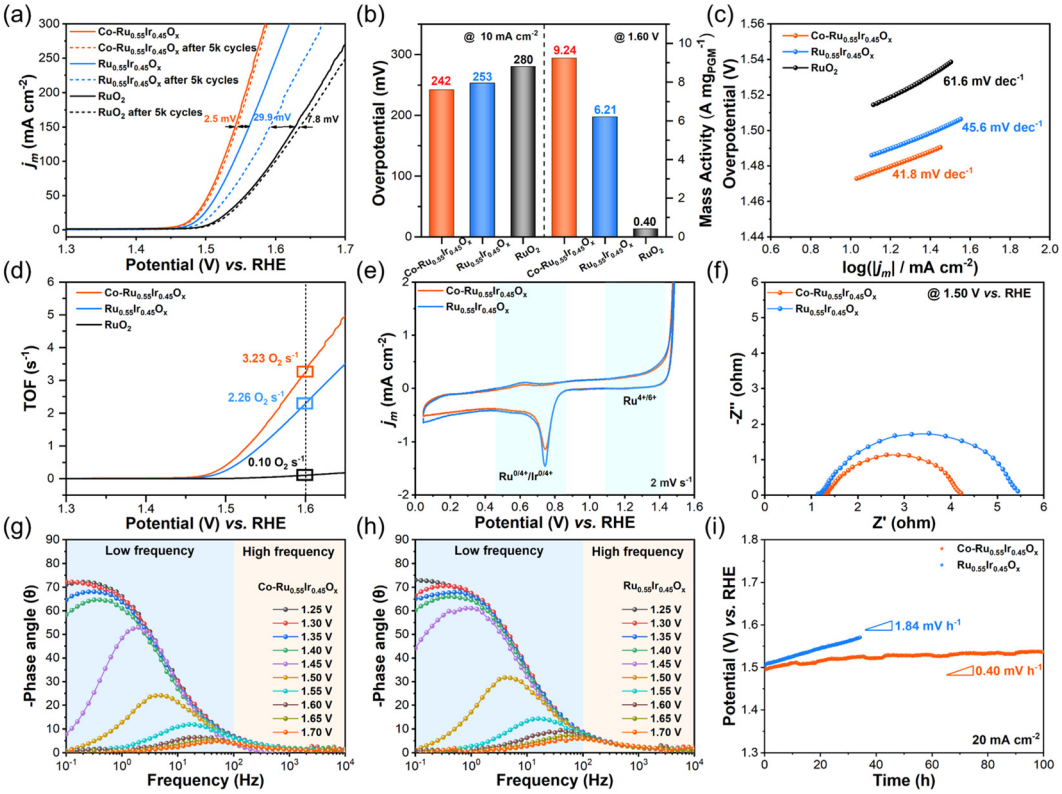

Fig. 4 Oxygen evolution reaction (OER) performance of Co-$Ru_{0.55}Ir_{0.45}O_x$ and $Ru_{0.55}Ir_{0.45}O_x$ in 1 M KOH solution: (a) polarization curves before and after 5k CV sweeps between 1.2 and 1.8 V (*vs.* RHE) at a scan rate of 100 mV s^{-1}. (b) Overpotential required to obtain 10 mA cm^{-2} (left panel) and the mass activity at the potential of 1.60 V *vs.* RHE (right panel) for Co-$Ru_{0.55}Ir_{0.45}O_x$, $Ru_{0.55}Ir_{0.45}O_x$ and commercial RuO_2. (c) Tafel slope and (d) turnover frequency. (e) Cyclic voltammetry of Co-$Ru_{0.55}Ir_{0.45}O_x$ and $Ru_{0.55}Ir_{0.45}O_x$ at a scan rate of 2 mV s^{-1}. (f) Nyquist plot at 1.50 V *vs.* RHE. Phase images in Bode plots of (g) Co-$Ru_{0.55}Ir_{0.45}O_x$ and (h) $Ru_{0.55}Ir_{0.45}O_x$ under different voltages. (i) Stability test recorded at a constant current density of 20 mA cm^{-2}.

5k cycles (Table S6). The results show that the concentrations of Ru and Ir in the solution were much lower for Co-$Ru_{0.55}Ir_{0.45}O_x$ after ADTs compared to $Ru_{0.55}Ir_{0.45}O_x$. This indicates that the Co dopants facilitated electron transfer from Co to Ir and Ru through d–d orbital hybridization, while electron transfer from Ir to Ru also occurred within the RuIr alloys. This prevented the excessive oxidation and dissolution of Ru/Ir species, thereby enhancing the stability of the catalyst. The Co element was also detected in the solution of Co-$Ru_{0.55}Ir_{0.45}O_x$, considering the mass percentages of Co, Ru, and Ir in Co-$Ru_{0.55}Ir_{0.45}O_x$, we found that the dissolution degree of Co was higher than that of Ru and Ir, indicating that Co preferentially leaches out during the OER process.

The CV curves reflect the evolution of the Ru/Ir species before the OER process (Fig. 4e). The redox peaks appearing at 0.45–0.85 V *vs.* RHE correspond to the oxidation–reduction evolution of $Ru^{0/4+}$ or $Ir^{0/4+}$.[38,39] The peak intensity for Co-$Ru_{0.55}Ir_{0.45}O_x$ was notably lower than that of $Ru_{0.55}Ir_{0.45}O_x$, suggesting that, as a result of electronic coupling, electrons from Co were transferred to Ir, and then to Ru. This sequential electron transfer effectively mitigates the over-oxidation of the Ru/Ir species. The peaks appearing at 1.10–1.40 V *vs.* RHE correspond to the redox peaks of $Ru^{4+/6+}$, at which point the Ru species undergo excessive oxidation to soluble RuO_4^{2-}, leading to irreversible dissolution. The oxidation peak of Co-$Ru_{0.55}Ir_{0.45}O_x$ was lower than that of $Ru_{0.55}Ir_{0.45}O_x$, demonstrating that Co dopants effectively prevent the dissolution of Ru during the OER process, thereby improving the structural stability of the Co-$Ru_{0.55}Ir_{0.45}O_x$.[40] The Nyquist plot shows that the R_{ct} of Co-$Ru_{0.55}Ir_{0.45}O_x$ at 1.50 V *vs.* RHE was 2.9 Ω, lower than 4.3 Ω of the $Ru_{0.55}Ir_{0.45}O_x$ catalyst, indicating its enhanced charge transfer capability (Fig. 4f). *Operando* EIS tests showed that Co-$Ru_{0.55}Ir_{0.45}O_x$ exhibited a consistently lower R_{ct} than $Ru_{0.55}Ir_{0.45}O_x$ across the entire OER operating range, indicating its superior reaction kinetics (Fig. S22). Furthermore, the Bode-phase plot revealed that, compared to $Ru_{0.55}Ir_{0.45}O_x$, Co-$Ru_{0.55}Ir_{0.45}O_x$ demonstrated a significant decrease in the phase angle at low frequencies (<100 Hz) within a range of 1.40–1.50 V *vs.* RHE, suggesting that Co doping enhances charge transfer at the electrode–electrolyte interface (Fig. 4g and h). During the OER process, both Co-$Ru_{0.55}Ir_{0.45}O_x$ and $Ru_{0.55}Ir_{0.45}O_x$ electrocatalysts undergo surface reconstruction, resulting in the formation of $Ru(Ir)O_2$ species that bind oxygen-containing intermediates excessively strongly, thus impeding the OER.[12,41] However, in Co-$Ru_{0.55}Ir_{0.45}O_x$, the preferential electrochemical dissolution of

Co induces the formation of cationic vacancies, which partially remove coordinated oxygen atoms from the surrounding Ru(Ir)O_2 species.[42] As a result, oxygen-deficient Ru/Ir–O_v species are generated and serve as the actual active sites for the OER.[34] The presence of Ru/Ir–O_v sites alters the OER mechanism from the traditional adsorbate evolution mechanism (AEM) to a metal site-oxygen vacancy synergistic mechanism (MS-O_vSM). In this pathway, two OH^- species nucleophilically attack the adjacent Ru/Ir–O_v pair and directly couple to form *O–O* intermediates, thereby circumventing the high formation energy required for the *OOH intermediate in the traditional AEM pathway. Consequently, the OER activity is significantly enhanced.[43]

Furthermore, Co-$Ru_{0.55}Ir_{0.45}O_x$ exhibited superior stability compared to $Ru_{0.55}Ir_{0.45}O_x$. After operating at a current density of 20 mA cm^{-2} for 100 h, Co-$Ru_{0.55}Ir_{0.45}O_x$ showed a much smaller increase in the overpotential (0.40 mV h^{-1}) compared to $Ru_{0.55}Ir_{0.45}O_x$ (1.84 mV h^{-1}, 30 h) (Fig. 4i). This exceptional stability was attributed to the d–d orbital interactions between Co and Ru/Ir, which facilitated the transfer of electrons from Co to Ir and Ru, thereby suppressing the dissolution of Ru/Ir species due to severe oxidation during the OER.

The XPS spectra obtained after the stability tests further support this conclusion. In both Co-$Ru_{0.55}Ir_{0.45}O_x$ and $Ru_{0.55}Ir_{0.45}O_x$ samples, the characteristic peaks of Ru 3p and Ir 4f orbitals shifted toward higher binding energies, indicating inevitable surface oxidation of Ru and Ir during the OER process, resulting in the formation of Ru^{n+} and Ir^{n+} species. For Co-$Ru_{0.55}Ir_{0.45}O_x$, the peaks corresponding to the Ru 3p exhibited a positive shift of 1.28 eV (Fig. 5a), whereas the characteristic Ru 3p signal in $Ru_{0.55}Ir_{0.45}$ disappeared entirely (Fig. 5b). This disappearance may be attributed to the excessive oxidation of Ru, leading to the formation of soluble RuO_4^{2-} and substantial leaching of Ru species into the electrolyte.[44] Similarly, the XPS spectra revealed that the peaks corresponding to the Ir 4f orbital in the Co-$Ru_{0.55}Ir_{0.45}O_x$ sample exhibited smaller shifts than those in $Ru_{0.55}Ir_{0.45}O_x$ (Fig. 5c and d). These findings suggest that the preferential leaching of Co, along with the electron delocalization induced by d–d orbital hybridization, effectively suppresses the over-oxidation and subsequent dissolution of Ru/Ir species during the OER process, thereby mitigating the loss of active sites and enhancing the stability of the catalyst.

As shown in Fig. 5e, the morphology of the Co-$Ru_{0.55}Ir_{0.45}O_x$ nanoparticles remained nearly unchanged after long-term operation. However, the HR-TEM image (Fig. 5f) revealed distinct lattice spacings of 0.222 nm and 0.227 nm, corresponding to the (101) facet of RuIr and the (200) facet of Ru/Ir–O, respectively. These observations were further supported by the fast Fourier transform (FFT) pattern (Fig. 5g). Combined with the CV curves (Fig. 4e), the results indicate that Ru/Ir species underwent partial transformation into Ru/Ir–O species during the OER process. Moreover, the EDS mappings (Fig. S23) showed a homogeneous distribution of Ru, Ir, and Co elements within the particles, confirming the structural stability of the Co-$Ru_{0.55}Ir_{0.45}O_x$ catalyst under OER conditions.

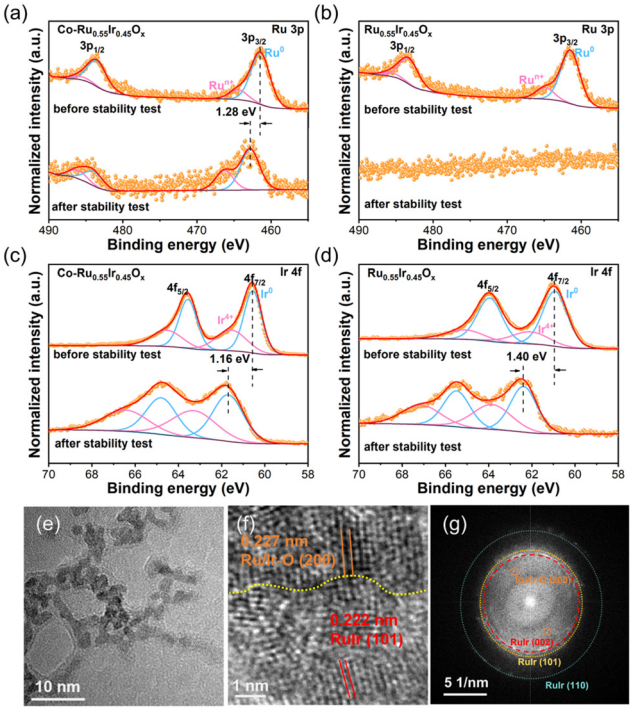

Fig. 5 XPS spectra of Ru 3p of (a) Co-$Ru_{0.55}Ir_{0.45}O_x$ and (b) $Ru_{0.55}Ir_{0.45}O_x$ before and after the OER stability test. XPS spectra of Ir 4f of (c) Co-$Ru_{0.55}Ir_{0.45}O_x$ and (d) $Ru_{0.55}Ir_{0.45}O_x$ before and after the OER stability test. TEM image (e), HR-TEM image (f) and relevant FFT (g) of Co-$Ru_{0.55}Ir_{0.45}O_x$ after the OER stability test.

Evaluation of overall water splitting performance

The overall water splitting performance was tested in a two-electrode system with a 1.0 M KOH electrolyte to evaluate the hydrogen production performance of Co-$Ru_{0.55}Ir_{0.45}O_x$ as a bifunctional catalyst. Fig. 6a shows the polarization curves for the three systems. The Co-$Ru_{0.55}Ir_{0.45}O_x$||Co-$Ru_{0.55}Ir_{0.45}O_x$ system exhibited a potential of 1.51 V at a current density of 10 mA cm^{-2}, which was lower than those of $Ru_{0.55}Ir_{0.45}O_x$||$Ru_{0.55}Ir_{0.45}O_x$ (1.53 V) and Pt/C||RuO_2 (1.55 V). Additionally, at a high current density of 200 mA cm^{-2}, the potential of the Co-$Ru_{0.55}Ir_{0.45}O_x$||Co-$Ru_{0.55}Ir_{0.45}O_x$ system remained below 1.70 V. The performance is comparable to those of the most advanced Ru/Ir-based bifunctional catalysts reported thus far (Fig. 6b and Table S7). This demonstrates the promising potential of Co-$Ru_{0.55}Ir_{0.45}O_x$ as a bifunctional catalyst for hydrogen production in water electrolysis. The long-term stability of overall water splitting was evaluated using the chronopotentiometry method. The Co-$Ru_{0.55}Ir_{0.45}O_x$||Co-$Ru_{0.55}Ir_{0.45}O_x$ system demonstrated superior activity and stability during continuous water electrolysis compared to the $Ru_{0.55}Ir_{0.45}O_x$||$Ru_{0.55}Ir_{0.45}O_x$ system, further confirming the important role of Co doping in maintaining catalyst stability (Fig. 6c, Fig. S24). Fig. S25 shows that when Co-$Ru_{0.55}Ir_{0.45}O_x$ was used as the catalyst in the

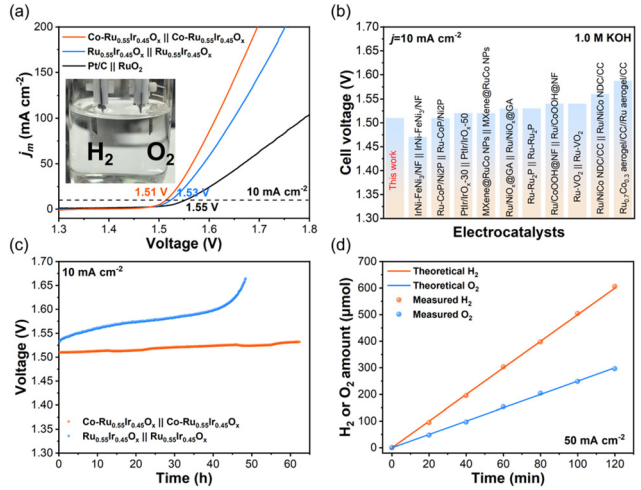

Fig. 6 Overall water splitting performance of Co-$Ru_{0.55}Ir_{0.45}O_x$ and $Ru_{0.55}Ir_{0.45}O_x$ in 1 M KOH solution: (a) polarization curves with Co-$Ru_{0.55}Ir_{0.45}O_x$ as both the anode and cathode catalyst at a scan rate of 10 mV s^{-1}. (b) Comparison cell voltage of overall water splitting at 10 mA cm^{-2} between Co-$Ru_{0.55}Ir_{0.45}O_x$||Co-$Ru_{0.55}Ir_{0.45}O_x$ and the advanced Ru/Ir-based electrocatalysts in 1.0 M KOH. (c) Chronopotentiometry tests of Co-$Ru_{0.55}Ir_{0.45}O_x$||Co-$Ru_{0.55}Ir_{0.45}O_x$ and $Ru_{0.55}Ir_{0.45}O_x$||$Ru_{0.55}Ir_{0.45}O_x$ pairs in 1 M KOH at 10 mA cm^{-2}. (d) Theoretical and experimental quantities of H_2 and O_2 generated by the Co-$Ru_{0.55}Ir_{0.45}O_x$ catalyst during overall water splitting at a current density.

H-cell for overall water splitting, the volume ratio of H_2 to O_2 collected *via* the drainage method was 2 : 1. In addition, the experimentally measured and theoretically calculated molar amounts of H_2 and O_2 during the overall water splitting process showed excellent agreement. This confirms that Co-$Ru_{0.55}Ir_{0.45}O_x$ almost achieves 100% faradaic efficiency, demonstrating its high energy conversion efficiency as a bifunctional electrocatalyst for water electrolysis (Fig. 6d).[45]

Conclusions

In summary, introducing Co dopants into RuIr alloys enhanced both the activity and stability of the catalysts for the alkaline HER and OER. For the HER, Co-$Ru_{0.55}Ir_{0.45}O_x$ required only a 21.2 mV overpotential to achieve a current density of 10 mA cm^{-2}. The Tafel slope of 27.9 mV dec^{-1} and TOF of 7.18 H_2 per s (at −0.15 V *vs.* RHE) demonstrate its fast reaction kinetics and excellent intrinsic activity. This improvement was attributed to Co dopants, which weakened the OH adsorption and optimized the hydrogen binding energy of Ru/Ir active sites, thereby exposing more active sites for water dissociation and facilitating the conversion of H_{ad} to H_2 *via* the Heyrovsky step. The boosted HER stability was due to the strong d–d orbital hybridization between Co and Ru/Ir atoms, which inhibited the aggregation and leaching of Ru/Ir atoms during the reaction process. For the OER, the improved activity of Co-$Ru_{0.55}Ir_{0.45}O_x$ (η = 242 mV at 10 mA cm^{-2}, Tafel slope = 41.8 mV dec^{-1}, TOF = 3.23 O_2 per s at 1.60 V *vs.* RHE) was attributed to the electrochemical dissolution of Co atoms and the enriched surface oxygen vacancies. These factors led to partial loss of coordinated oxygen from surrounding Ru(Ir)O_2 and the formation of oxygen-deficient Ru/Ir–O_v species. These Ru/Ir–O_v species serve as the actual OER active sites and activate a metal site–oxygen vacancy synergistic mechanism (MS-O_vSM), wherein two OH^- nucleophilically attack the adjacent Ru/Ir–O_v pair to form *O–O* intermediates directly, thus significantly enhancing OER activity. Moreover, the d–d orbital interaction between Co dopants and Ru/Ir facilitated the electron transfer from Co to Ir and Ru, thereby inhibiting the leaching of Ru/Ir species due to over-oxidation, which enhanced OER stability. Additionally, the constructed Co-$Ru_{0.55}Ir_{0.45}O_x$||Co-$Ru_{0.55}Ir_{0.45}O_x$ electrolyzer achieved a current density of 10 mA cm^{-2} at a lower potential of 1.51 V and remained stable for over 60 h at different current densities.

Conflicts of interest

There are no conflicts to declare.

Data availability

Data supporting the findings in the present work are available in the manuscript or SI. Additional data are available from the corresponding authors upon reasonable request.

Supplementary information is available. See DOI: **https://doi.org/10.1039/d5nr02238j**.

Acknowledgements

We sincerely appreciate the support provided by the following funding sources: the National Key R&D Program of China (2021YFB2400400), the National Natural Science Foundation of China (Grant No. 22409157 and 22379120), the Key Research and Development Plan of Shanxi Province (China, Grant No. 2018ZDXM-GY-135 and 2021JLM-36), the China Postdoctoral Science Foundation (2020M673408), the Higher Education Institution Academic Discipline Innovation and Talent Introduction Plan ("111 Plan") (No. B23025), the Fundamental Research Funds for the "Young Talent Support Plan" of Xi'an Jiaotong University (HG6J003), and the "1000-Plan Program" of Shaanxi Province.

References

1 P. Zhang, M. Gan, Y. Song, P. Liu, H. Liang, Y. Shen, B. Xu, T. Liao, J. Guo and Z. Sun, Bifunctional Pt dual atoms for overall water splitting, *Appl. Catal., B*, 2024, **355**, 124214.
2 X. Zhang, Y. Guo and C. Wang, Multi-interface engineering of nickel-based electrocatalysts for alkaline hydrogen evolution reaction, *Energy Mater.*, 2024, **4**, 400044.

3 Y. Shi, L. Song, Y. Liu, T. Wang, C. Li, J. Lai and L. Wang, Dual Cocatalytic Sites Synergize NiFe Layered Double Hydroxide to Boost Oxygen Evolution Reaction in Anion Exchange Membrane Water Electrolyzer, *Adv. Energy Mater.*, 2024, **14**, 2402046.
4 Z. F. Gan, C. Y. Shu, C. W. Deng, W. Du, B. Huang and W. Tang, Confinement of Pt NPs by hollow-porous-carbon-spheres pore regulation with promoted activity and durability in the hydrogen evolution reaction, *Nanoscale*, 2021, **13**, 18273–18280.
5 Y. Zhu, S. Zhang, R. Chen, Z. Wang, W. Wu, H. Jiang, H. Chen and N. Cheng, Controllable Electronic Transfer Tailoring d–band Center via Cobalt–Oxygen–Bridged Ru/Fe Dual–sites for Boosted Oxygen Evolution, *Small*, 2024, **20**, 2310611.
6 M. Li, X. Wang, K. Liu, Z. Zhu, H. Guo, M. Li, H. Du, D. Sun, H. Li, K. Huang, Y. Tang and G. Fu, Ce–Induced Differentiated Regulation of Co Sites via Gradient Orbital Coupling for Bifunctional Water–Splitting Reactions, *Adv. Energy Mater.*, 2023, **13**, 2301162.
7 P. Wang, K. Wang, Y. Liu, H. Li, Y. Guo, Y. Tian, S. Guo, M. Luo, Y. He, Z. Liu and S. Guo, Dual–Type Ru Atomic Sites for Efficient Alkaline Overall Water Splitting, *Adv. Funct. Mater.*, 2024, **34**, 2316709.
8 T. Luo, J. Huang, Y. Hu, C. Yuan, J. Chen, L. Cao, K. Kajiyoshi, Y. Liu, Y. Zhao, Z. Li and Y. Feng, Fullerene Lattice–Confined Ru Nanoparticles and Single Atoms Synergistically Boost Electrocatalytic Hydrogen Evolution Reaction, *Adv. Funct. Mater.*, 2023, **33**, 2213058.
9 Y. Chen, Y. Lee, W. Chu and J. Li, Trace Ru-tuned NiO/CNT electrocatalysts outperform benchmark Pt for alkaline hydrogen evolution with superior mass activity, *Chem. Eng. J.*, 2023, **472**, 144922.
10 Z. Gan, C. Shu, J. Cao, Z. Chen, P. Qiu, Z. Chen, X. Wang, Y. Wu, S. Wang, X. Yang and W. Tang, P–Doping Modulated RuIr Nanoparticles Anchored on Co/N/C Catalysts with Improved Alkaline Hydrogen Evolution Activity and Stability, *Small*, 2024, **21**, 2408887.
11 X. Kong, J. Xu, Z. Ju and C. Chen, Durable Ru Nanocrystal with HfO2 Modification for Acidic Overall Water Splitting, *Nano-Micro Lett.*, 2024, **16**, 185.
12 J. Feng, F. Lv, W. Zhang, P. Li, K. Wang, C. Yang, B. Wang, Y. Yang, J. Zhou, F. Lin, G. C. Wang and S. Guo, Iridium–Based Multimetallic Porous Hollow Nanocrystals for Efficient Overall–Water–Splitting Catalysis, *Adv. Mater.*, 2017, **29**, 1703798.
13 Y. Yu, H. Xu, X. Xiong, X. Chen, Y. Xiao, H. Wang, D. Wu, Y. Hua, X. Tian and J. Li, Ultra–Thin RuIr Alloy as Durable Electrocatalyst for Seawater Hydrogen Evolution Reaction, *Small*, 2024, **20**, 2405784.
14 Y. Li, L. Zhao, X. Du, W. Gao, C. Zhang, H. Chen, X. He, C. Wang and Z. Mao, Cobalt-doped IrRu bifunctional nanocrystals for reversal-tolerant anodes in proton-exchange membrane fuel cells, *Chem. Eng. J.*, 2023, **461**, 141823.
15 N. Danilovic, R. Subbaraman, K. C. Chang, S. H. Chang, Y. Kang, J. Snyder, A. P. Paulikas, D. Strmcnik, Y. T. Kim, D. Myers, V. R. Stamenkovic and N. M. Markovic, Using Surface Segregation To Design Stable Ru–Ir Oxides for the Oxygen Evolution Reaction in Acidic Environments, *Angew. Chem., Int. Ed.*, 2014, **53**, 14016–14021.
16 T. Hrbek, P. Kúš, J. Drnec, M. Mirolo, H. Nedumkulam, I. Martens, J. Nováková, T. Skála and I. Matolínová, Strain–Engineered Ir Shell Enhances Activity and Stability of Ir–Ru Catalysts for Water Electrolysis: An Operando Wide–Angle X–Ray Scattering Study, *Adv. Energy Mater.*, 2024, **15**, 2403738.
17 J. Shan, C. Guo, Y. Zhu, S. Chen, L. Song, M. Jaroniec, Y. Zheng and S.-Z. Qiao, Charge-Redistribution-Enhanced Nanocrystalline Ru@IrOx Electrocatalysts for Oxygen Evolution in Acidic Media, *Chem*, 2019, **5**, 445–459.
18 L. Chong, J. Wen, E. Song, Z. Yang, I. D. Bloom and W. Ding, Synergistic Co–Ir/Ru Composite Electrocatalysts Impart Efficient and Durable Oxygen Evolution Catalysis in Acid, *Adv. Energy Mater.*, 2023, **13**, 2302306.
19 X. Chen, L. Ye, W. Wu, S. Chen, Z. Wang, Y. Zhu, H. Jiang, R. Chen and N. Cheng, Compressed Ru skin on atomic-ordered hexagonal Ru-Ni enabling rapid Volmer-Tafel kinetics for efficient alkaline hydrogen evolution, *Chem. Eng. J.*, 2024, **487**, 150457.
20 M. Xiao, W. Xu, R. Li, Y. Sun, J. Liu, F. Liu, J. Gan and S. Gao, Lotus root-like RuIr alloys with close-packed (0001) branches: Strain-driven performance for acidic water oxidation, *J. Energy Chem.*, 2024, **92**, 579–590.
21 J.-J. Velasco-Vélez, E. A. Carbonio, C.-H. Chuang, C.-J. Hsu, J.-F. Lee, R. Arrigo, M. Hävecker, R. Wang, M. Plodinec, F. R. Wang, A. Centeno, A. Zurutuza, L. J. Falling, R. V. Mom, S. Hofmann, R. Schlögl, A. Knop-Gericke and T. E. Jones, Surface Electron-Hole Rich Species Active in the Electrocatalytic Water Oxidation, *J. Am. Chem. Soc.*, 2021, **143**, 12524–12534.
22 W. He, W. Feng and Z. Sun, Manipulating the interfacial water structure by electron redistribution for the hydrogen evolution reaction, *Nanoscale*, 2024, **16**, 18518–18523.
23 Y. Xie, Y. Feng, S. Pan, H. Bao, Y. Yu, F. Luo and Z. Yang, Electrochemical Leaching of Ni Dopants in IrRu Alloy Electrocatalyst Boosts Overall Water Splitting, *Adv. Funct. Mater.*, 2024, **34**, 2406351.
24 Q. He, Y. Zhou, H. Shou, X. Wang, P. Zhang, W. Xu, S. Qiao, C. Wu, H. Liu, D. Liu, S. Chen, R. Long, Z. Qi, X. Wu and L. Song, Synergic Reaction Kinetics over Adjacent Ruthenium Sites for Superb Hydrogen Generation in Alkaline Media, *Adv. Mater.*, 2022, **34**, 2110604.
25 J. Zhao, M. Kou, Q. Yuan, Y. Yuan and J. Zhao, Hydrogen Spillover–Bridged Interfacial Water Activation of WCx and Hydrogen Recombination of Ru as Dual Active Sites for Accelerating Electrocatalytic Hydrogen Evolution, *Small*, 2024, **21**, 2406022.
26 Q. Mao, S. Jiao, K. Ren, S. Wang, Y. Xu, Z. Wang, X. Li, L. Wang and H. Wang, Transition metal and phosphorus co-doping induced lattice strain in mesoporous Rh-based nanospheres for pH-universal hydrogen evolution electrocatalysis, *Chem. Eng. J.*, 2021, **426**, 131227.

27 H. Wang, Y. Jiao, G. Zhang, W. Ma, W. Fan, X. Liu, Y. Zhao, H. Xie, W. Ma and X. Zong, Stabilizing Electron–Deficient Ru Nanoclusters via Strong Electronic Metal–Support Interaction for Practical Anion–Exchange Membrane Electrolyzer, *Adv. Funct. Mater.*, 2024, **35**, 2418617.
28 S. E. Islam, D.-R. Hang, C.-T. Liang, K. H. Sharma, H.-C. Huang and M. M. C. Chou, Tuning the electrocatalytic activity of MoS2 nanosheets via the in situ hybridization with ruthenium and graphene network, *Chem. Eng. J.*, 2024, **488**, 150950.
29 J. Chen, G. Qian, H. Zhang, S. Feng, Y. Mo, L. Luo and S. Yin, PtCo@PtSn Heterojunction with High Stability/Activity for pH–Universal H2 Evolution, *Adv. Funct. Mater.*, 2021, **32**, 2107597.
30 X. Wang, H. Yao, C. Zhang, C. Li, K. Tong, M. Gu, Z. Cao, M. Huang and H. Jiang, Double–Tuned RuCo Dual Metal Single Atoms and Nanoalloy with Synchronously Expedited Volmer/Tafel Kinetics for Effective and Ultrastable Ampere–Level Current Density Hydrogen Production, *Adv. Funct. Mater.*, 2023, **33**, 2301804.
31 R. Yao, K. Sun, K. Zhang, Y. Wu, Y. Du, Q. Zhao, G. Liu, C. Chen, Y. Sun and J. Li, Stable hydrogen evolution reaction at high current densities via designing the Ni single atoms and Ru nanoparticles linked by carbon bridges, *Nat. Commun.*, 2024, **15**, 2218.
32 J. Zhu, J. Chi, X. Wang, T. Cui, L. Guo, B. Dong, X. Liu and L. Wang, Boosting hydrogen evolution reaction activity of Ru anchored binary oxyhydroxide by F-doping in alkaline seawater, *Nano Energy*, 2024, **121**, 109249.
33 L. Wang, Z. Xu, C. H. Kuo, J. Peng, F. Hu, L. Li, H. Y. Chen, J. Wang and S. Peng, Stabilizing Low-Valence Single Atoms by Constructing Metalloid Tungsten Carbide Supports for Efficient Hydrogen Oxidation and Evolution, *Angew. Chem., Int. Ed.*, 2023, **62**, e202311937.
34 J. Shan, T. Ling, K. Davey, Y. Zheng and S. Z. Qiao, Transition–Metal–Doped RuIr Bifunctional Nanocrystals for Overall Water Splitting in Acidic Environments, *Adv. Mater.*, 2019, **31**, 1900510.
35 Y. Yuan, H. Fang, K. Chen, J. Huang, J. Chen, Z. Lu, H. Wang, Z. Zhao, W. Chen and Z. Wen, Engineering High–Density Grain Boundaries in Ru0.8Ir0.2Ox Solid–Solution Nanosheets for Efficient and Durable OER Electrocatalysis, *Adv. Mater.*, 2025, **37**, 2501607.
36 S. Chen, S. Zhang, L. Guo, L. Pan, C. Shi, X. Zhang, Z.-F. Huang, G. Yang and J.-J. Zou, Reconstructed Ir-O-Mo species with strong Brønsted acidity for acidic water oxidation, *Nat. Commun.*, 2023, **14**, 4127.
37 B. Lu, C. Wahl, R. dos Reis, J. Edgington, X. K. Lu, R. Li, M. E. Sweers, B. Ruggiero, G. T. K. K. Gunasooriya, V. Dravid and L. C. Seitz, Key role of paracrystalline motifs on iridium oxide surfaces for acidic water oxidation, *Nat. Catal.*, 2024, **7**, 868–877.
38 H. Liu, Z. Zhang, J. Fang, M. Li, M. G. Sendeku, X. Wang, H. Wu, Y. Li, J. Ge, Z. Zhuang, D. Zhou, Y. Kuang and X. Sun, Eliminating over-oxidation of ruthenium oxides by niobium for highly stable electrocatalytic oxygen evolution in acidic media, *Joule*, 2023, **7**, 558–573.
39 Y. Wen, C. Liu, R. Huang, H. Zhang, X. Li, F. P. García de Arquer, Z. Liu, Y. Li and B. Zhang, Introducing Brønsted acid sites to accelerate the bridging-oxygen-assisted deprotonation in acidic water oxidation, *Nat. Commun.*, 2022, **13**, 4871.
40 N. Xu, M.-M. Li, H.-Y. Sun, G. Li, X. Wen, D. Ouyang, C.-Y. Liu, Y.-M. Chai and B. Dong, Atmosphere-driven oriental regulation of Ru valence for boosting alkaline water electrolysis, *Chem. Eng. J.*, 2024, **502**, 158051.
41 T. Reier, Z. Pawolek, S. Cherevko, M. Bruns, T. Jones, D. Teschner, S. Selve, A. Bergmann, H. N. Nong, R. Schlögl, K. J. J. Mayrhofer and P. Strasser, Molecular Insight in Structure and Activity of Highly Efficient, Low-Ir Ir–Ni Oxide Catalysts for Electrochemical Water Splitting (OER), *J. Am. Chem. Soc.*, 2015, **137**, 13031–13040.
42 Y. Liu, M. Zhang, C. Zhang, H. Zhang and H. Wang, An IrRuOx catalyst supported by oxygen-vacant Ta oxide for the oxygen evolution reaction and proton exchange membrane water electrolysis, *Nanoscale*, 2024, **16**, 9382–9391.
43 M. Liu, X. Zhong, X. Chen, D. Wu, C. Yang, S. Li, C. Ni, Y. Chen, Q. Liu and H. Su, Unraveling Compressive Strain and Oxygen Vacancy Effect of Iridium Oxide for Proton–Exchange Membrane Water Electrolyzers, *Adv. Mater.*, 2025, **37**, 2501179.
44 G. Zhao, W. Guo, M. Shan, Y. Fang, G. Wang, M. Gao, Y. Liu, H. Pan and W. Sun, Metallic Ru–Ru Interaction in Ruthenium Oxide Enabling Durable Proton Exchange Membrane Water Electrolysis, *Adv. Mater.*, 2024, **36**, 2404213.
45 Y. Hou, Z. Qin, X. Han, Y. Liu, W. Zhang, X. Cao, Y. Cao, J.-P. Lang and H. Gu, Thermal evaporation-driven fabrication of Ru/RuO2 nanoparticles onto nickel foam for efficient overall water splitting, *Nanoscale*, 2024, **16**, 6662–6668.

